Enhancing thermoelectric output in a molecular heat engine utilizing Yu-Shiba-Rusinov bound states

Serhii Volosheniuk [1], Damian Bouwmeester[1], David Vogel[2],
Christina Wegeberg[2,3], Chunwei Hsu [1], Marcel Mayor [2,4,5],
Herre S. J. van der Zant [1] ✉ & Pascal Gehring [6] ✉

Particle exchange heat engines are a novel class of cyclic heat engines that are all-electrical, contain no moving parts and can therefore be scaled down to nanometer size. At the center of their operation is the manipulation of a particle flow between a hot and a cold reservoir through energy filtering mechanisms, where their efficiency depends primarily on the sharpness of the energy filter. In this study, we investigate the efficiency enhancement of such engines by utilizing ultra-sharp transmission resonances formed by magnetic impurities interacting with superconductors, known as Yu-Shiba-Rusinov bound states. To this end, we couple a neutral and stable diradical molecule to superconducting break-junction electrodes, and study its thermoelectric properties at ultra-low temperatures. By driving the molecular heat engine through a phase transition from a Kondo state into the Yu-Shiba-Rusinov regime, we observe a five fold increase in the thermoelectric power factor. This observation could pave the way for practical applications such as cryogenic waste heat recovery and efficient spot-cooling for future quantum computing architectures.

Conventional cyclic heat engines contain moving parts, making them prone to failure and render them unpractical for sensing, for wearable devices or for extraterrestrial applications[1]. In contrast, particle exchange heat engines[2] offer a promising alternative, operating without moving components by exchanging particles, such as photons or electrons, between two heat reservoirs. Their working principle is based on energy filtering of particles, where a high engine efficiency could be achieved if a narrow energy band – compared to the thermal energy $k_B T$ – for particle exchange between reservoirs is maintained to prevent entropy generation during particle transfer[3]. For example, quantum dots (QDs) tunnel-coupled to two electron reservoirs have been demonstrated to serve as precise energy filters, producing efficiencies close to the lower Curzon-Ahlborn limit[4]. Quantum systems coupled to superconductors offer a promising alternative pathway to achieve energy filtering[5]. A variety of physical phenomena including Andreev reflections[6], multiple Andreev reflection[7], and Cooper pair splitting[8,9] have been studied under different conditions. Special emphasis has been placed on the interplay between a superconductor and a magnetic moment on a quantum dot. This interplay is similar to a normal metal-impurity connection, where electrons in the metal actively screen the impurity, thus giving rise to the Kondo effect[10]. In case of a coupled superconductor-quantum dot system, superconducting phenomena compete with Kondo screening. This competition can be revealed through the formation of sharp Yu-Shiba-Rusinov (YSR) bound states induced inside the superconductor gap[11–13].

[1]Kavli Institute of Nanoscience, Delft University of Technology, Delft, The Netherlands. [2]Department of Chemistry, University of Basel, Basel, Switzerland. [3]Department of Chemistry, Lund University, Lund, Sweden. [4]Institute for Nanotechnology (INT), Karlsruhe Institute of Technology (KIT), Karlsruhe, Germany. [5]Lehn Institute of Functional Materials (LIFM), Sun Yat-Sen University (SYSU), Guangzhou, China. [6]IMCN/NAPS, Université catholique de Louvain, Louvain-la-Neuve, Belgium. ✉e-mail: H.S.J.vanderZant@tudelft.nl; pascal.gehring@uclouvain.be

So far, studies exploring Yu-Shiba-Rusinov (YSR) states have primarily utilized scanning tunneling spectroscopy (STS)[14–16], focusing on magnetic atoms and molecules coupled to superconducting substrates. STS has enabled the investigation of YSR state hybridization[17,18], the identification of various sub-gap excitations, and the tuning of quantum phase transitions by adjusting the tip-substrate distance[19].

In this work we explore if sharp features in the density of states created by YSR bound states can serve as efficient energy filters to enhance the performance of a molecular heat engine. To this end, we measured a diradical nitronyl nitroxide compound (NNDR) molecule in a three-terminal device with proximity-induced superconducting leads. The subject of study behaves as a spin-1/2 system with a large charging energy. The induced superconductivity leads to the existence of in-gap bound states. We were able to tune the system from a magnetic doublet ground state to a Kondo singlet by applying an external magnetic field and to a BCS-like singlet by changing the number of electrons on the molecule. We find that this phase transition enhances the thermoelectric power factor – a quantity proportional to the

efficiency of the molecular particle exchange heat engines – by a factor of five.

Results

To investigate the performance of the molecular particle exchange heat engine we measure its electrical and thermoelectric properties at the same time, and at millikelvin temperatures, by using our recently developed device architecture[20,21] whose working principle is shown in Fig. 1a. To this end, we electrically and thermally bias the junction simultaneously using an ac bias voltage V_{ac} at frequency ω_1 and an ac heater current $\tilde{I}_H$ at ω_2. At the source terminal we then demodulate the resulting ac current at ω_1 and $2\omega_2$ to access both the differential conductance $dI/dV = \tilde{I}_{ac}/V_B$ and the thermocurrent I_{th} (see Methods for more details). For the molecule, an all-organic NNDR is used (Fig. 1b), which is a stable diradical (see details in Methods). As will be shown later, by applying a negative gate voltage V_G, one electron can be removed from the molecule and it then acts as a spin-1/2 system.

The superconducting contacts used in this study serve a dual purpose as they are used as thermometers[21] and allow to induce
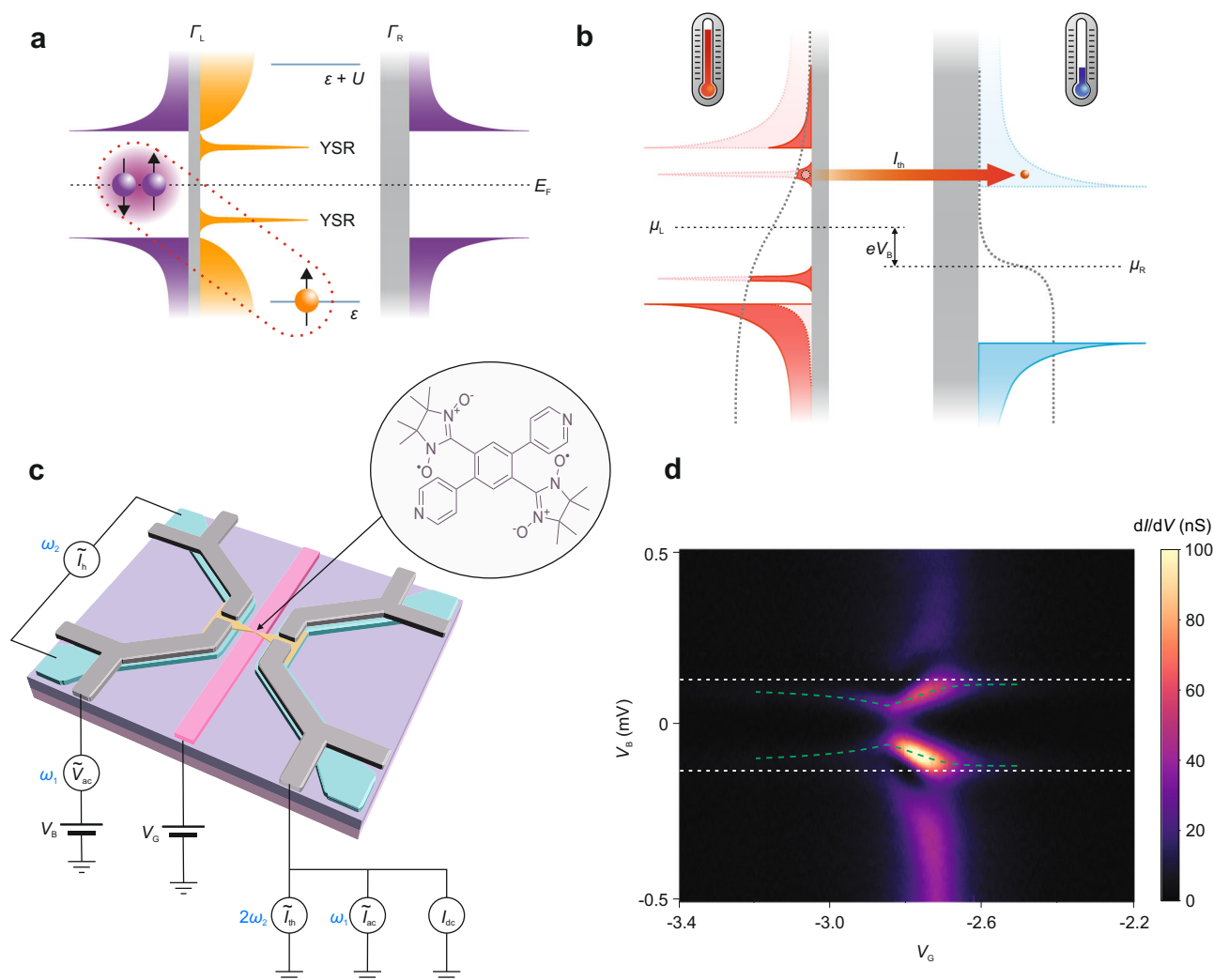

Fig. 1 | A molecular heat engine in the YSR regime. a Sketch of a superconductor-quantum dot-superconductor (S-QD-S) system. An unpaired spin (orange sphere) residing on the QD, in our case a single molecule, couples to a Cooper pair (purple spheres) inside the proximitized gold leads forming YSR bound states. **b** Energy filtering via YSR states. A thermoelectric current I_{th} (red arrow) is flowing from the left (hot) side to the right (cold) side. The grey dotted lines depict the Fermi-Dirac distribution functions of the leads. **c** Schematic of the thermopower device (back gate electrode (pink), heaters (light blue), golden bridge (yellow), superconducting

contacts (grey)). The circuit diagram indicates which terminals are used to apply a gate voltage V_G, a dc bias voltage V_B, an ac bias voltage V_{ac} (ω_1) and an ac heater current I_h (ω_2), and which terminals are used to measure the dc I_{dc}, the ac I_{ac} (ω_1) and the thermocurrent I_{th} (ω_2). The insert shows the structure of the Nitronyl nitroxide diradical molecule (NNDR) which posseses two free spins on the oxygen atoms. **d** Map of the differential conductance as a function of gate and bias voltage recorded at 62 mK. The bound states and the superconducting gap are highlighted by green and white dotted lines, respectively.
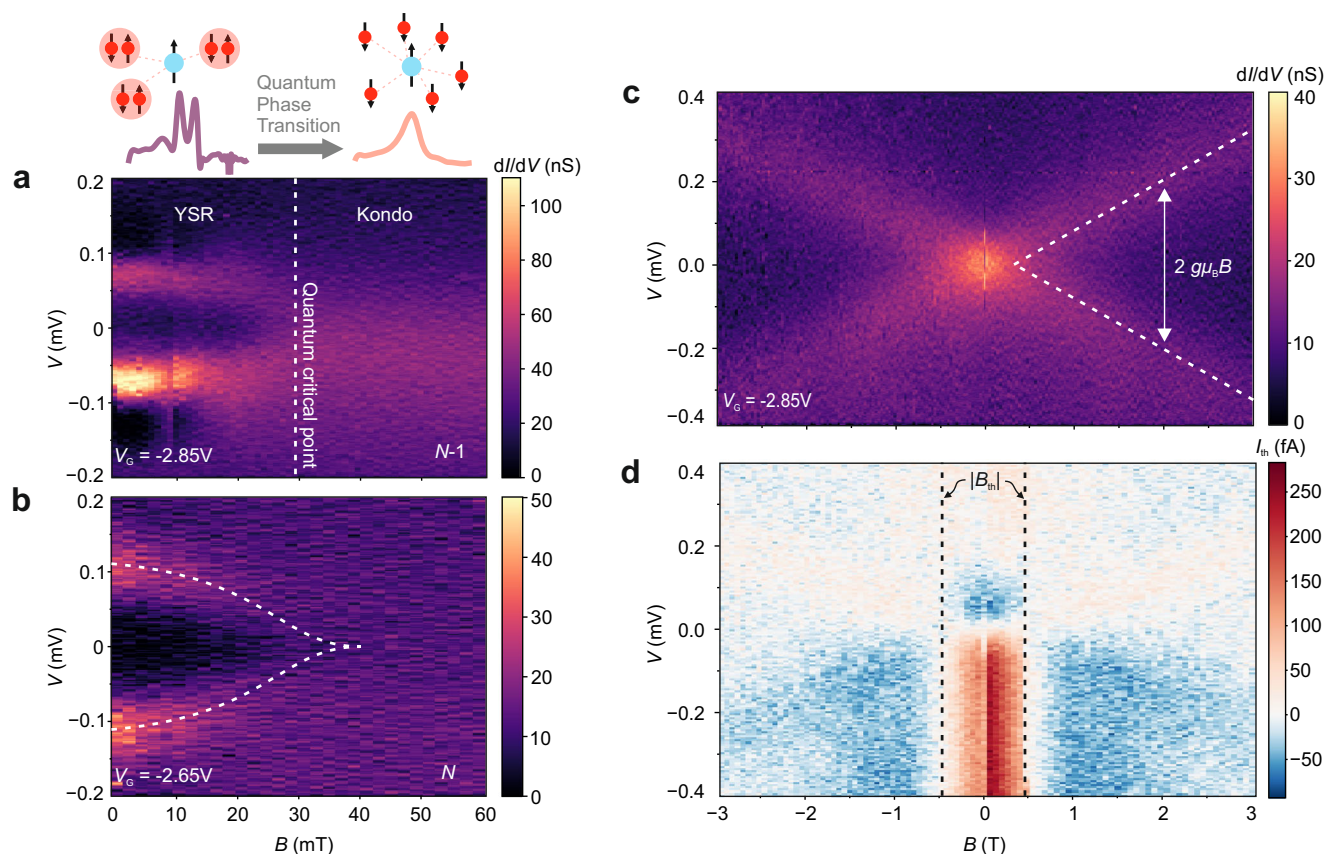
Fig. 2 | Study of quantum phase transitions by magnetic field dependent electrical and thermoelectric transport. a, b Differential conductance as a function of bias voltage and magnetic field at $V_G = -2.85$ V (**a**) and $V_G = -2.65$ V (**b**), respectively. **c, d** Differential conductance (**c**) and thermocurrent (**d**) measured simultaneously as a function of bias voltage and magnetic field. The white dotted line indicates the Zeeman splitting of the Kondo resonance that occurs at a field of $B_{th} = 0.49$ T (vertical black dotted lines).

proximity superconductivity in the molecular junction (see Fig. S24) which leads to a competition between Kondo screening (characterized by the Kondo temperature, T_K) and superconducting pairing (characterized by the gap energy, $\Delta = (\Delta_1 + \Delta_2)/2$, where Δ_1 and Δ_2 are source and drain gap energy respectively). As depicted in Fig. 1c, the coupling of a spin-1/2 impurity (i.e., the molecule) to the superconducting electrodes yields the formation of bound states inside the superconducting gap as quasi-particles try to screen the spin of the impurity.

Figure 1d shows a detailed V_B and V_G map of dI/dV around the charge degeneracy point (CDP) recorded at a temperature of 62 mK. Two horizontal lines (highlighted by white dotted guidelines for the eye in Fig. 1d) indicate the voltage at which the coherence peaks of the source and the drain overlap, with their respective gap energies Δ_1 and Δ_2 (where $\Delta_1 + \Delta_2 \approx 130\,\mu$eV). When V_G is decreased below -2.8 V, the charge ground state changes from N to $N-1$ and the molecule is in the spin-1/2 state (see also Fig. S21). As we find only one CDP in the accessible gate range, the charging energy, E_C, is much larger than the other relevant energy scales (Δ, T_K, Γ). Furthermore, two excited state lines at $V = 90\,\mu$V in the $N-1$ and at $V = 120\,\mu$V in the N charge state, respectively, merge near the charge degeneracy point. We attribute the bound state to a YSR state since the electronic coupling to the leads in our device is highly asymmetric and $\Delta \gtrsim T_K$ (see discussion of Fig. 2 below). The bound state undergoes a phase transition and changes its ground and excited state when increasing V_G and changing the charge state to N (see discussion below). When going through this transition, the gap between bound states at positive and negative bias voltage decreases to 100 μeV – without a complete closing – which is the typical behaviour of a superconductor-quantum dot-superconductor system.

An external out-of-plane magnetic field is expected to suppress Cooper pairing while favouring Kondo screening. In Fig. 2a the differential conductance as a function of bias voltage and magnetic field, at constant $V_G = -2.85$ V (left hand side of CDP, $N-1$) is depicted. Around zero magnetic field two differential conductance peaks which we attribute to the YSR states are visible: one at positive and one at negative bias. The voltage difference between the two peak positions stays almost constant up to a field of 10 mT and decreases – due to a change of the exchange coupling J and Δ with magnetic field – in the range between 10 mT and 30 mT, where the two peaks merge and form a single zero-bias peak. We attribute this zero-bias peak to a Kondo resonance. The continuous evolution between the two competing ground states of the system, which can be triggered at nearly zero temperature, is a hallmark for quantum criticality[22]. For our molecular junction we observe that the quantum phase transition, driven by the external magnetic field, has a quantum critical point at ≈ 30 mT. Such quantum phase transition of the molecular quantum dot is absent in the N charge state ($V_G = -2.65$ V, see Fig. 2b): the in-gap bound states are closing with the magnetic field and disappear completely, indicating the transition of the proximitized gold electrodes to their normal state. Furthermore, the presence/absence of a Kondo resonance on the left/right hand side of the CDP, respectively, allows us to conclude that an unpaired electron resides on the molecule in the $N-1$ charge state.

In Fig. 2c, d we show the V_B and high B-field dependence of the differential conductance and thermocurrent measured simultaneously at $V_G = -2.85$ V. The Kondo resonance starts to Zeeman split at a magnetic field of $B_{th} = 0.49$ T. At the same time, the slope dI_{th}/dV of the thermocurrent at zero bias changes sign. We have shown recently[23]
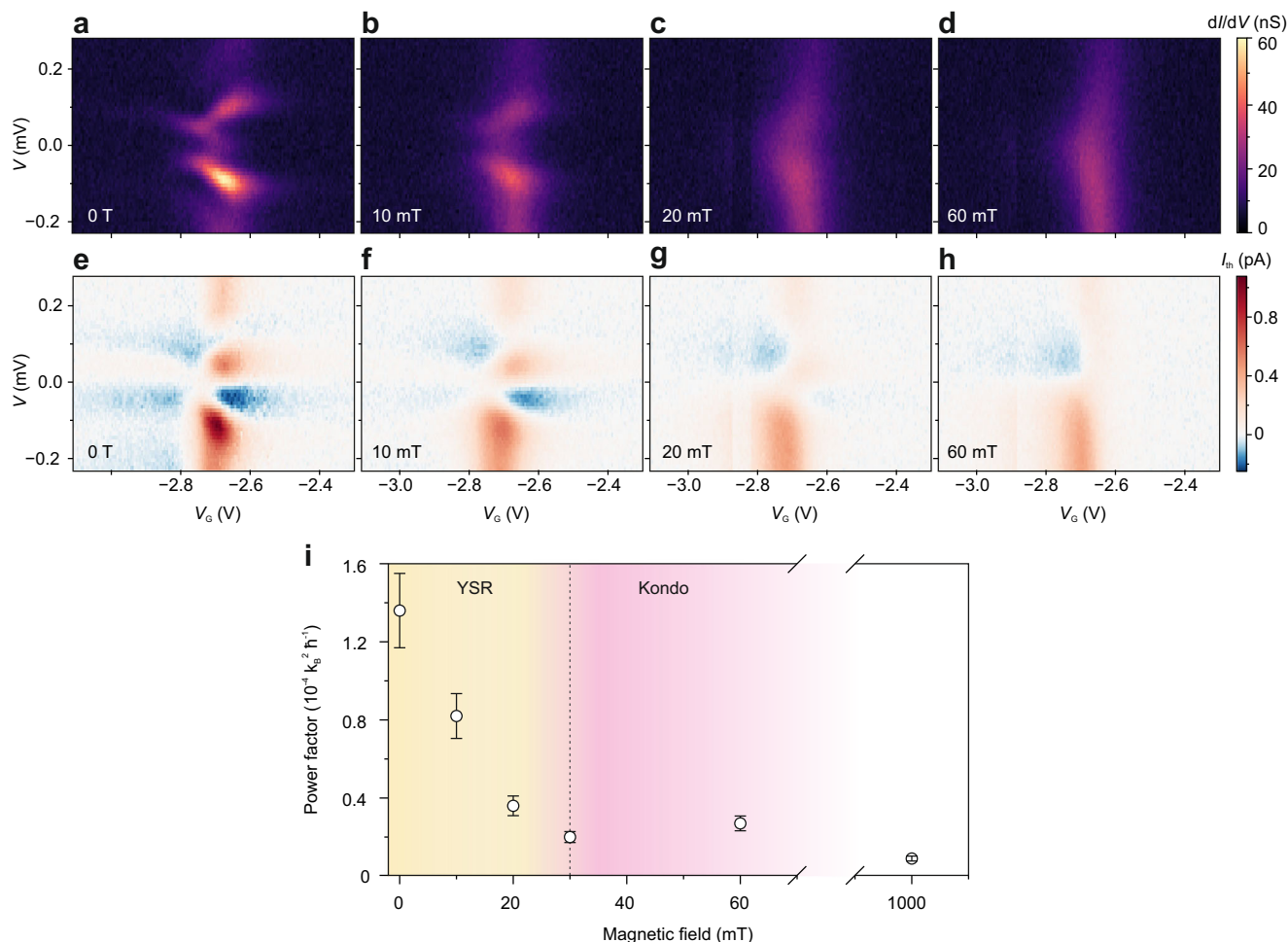
Fig. 3 | Enhancement of thermoelectric output of a molecular heat engine by YSR states. a–d Maps of differential conductance and (**e–h**), thermocurrent measured simultaneously as a function of bias and back gate voltage at different magnetic fields (0, 10, 20, and 60 mT, respectively). **i** Thermoelectric power factor $S_0^2 G$ as a function of magnetic field. The error bars were calculated using $\Delta PF = PF \sqrt{2} \frac{\Delta(T_H - T_C)}{T_H - T_C}$, where $\Delta(T_H - T_C)$ is the uncertainty of the temperature bias that results from thermometry measurements.

that the magnetic field B_{th} at which this sign-change occurs, can be used to accurately extract the Kondo temperature $T_K = \frac{4}{3}\frac{\mu_B B_{th}}{k_B}$, where k_B is the Boltzmann constant and μ_B is the Bohr magneton. We find $T_K = 0.8 \pm 0.1$ K, which agrees well with the value estimated from the width of the Kondo peak (0.73 ± 0.04 K, see Fig. S20). Furthermore, from the Zeeman splitting at high magnetic fields (dotted line in Fig. 2c) we conclude that the junction is a spin-1/2 system with a g factor of 2 (see more details and Kondo analysis in supplementary materials).

To further study how the quantum phase transition between the YSR and the Kondo regime impacts the thermoelectric properties of the single-molecule particle exchange heat engine, we simultaneously recorded maps of the bias and gate voltage dependent differential conductance and thermocurrent at a temperature of 150 mK for different applied magnetic fields between 0 and 60 mT (Fig. 3 and Figs. S25–S34). For zero magnetic field, the differential conductance map (see Fig. 3a) resembles that shown in Fig. 1d; YSR bound states can be observed on the left/right hand side of the CDP, respectively. There is a small asymmetry between the differential conductance at positive and negative bias voltage with peak heights in the range of 2 to 62 nS for the upper arc and 2 to 108 nS for the lower one, which do not exceed the upper bound ($\frac{2e^2}{h}$) of the theoretical expectations for YSR[24]. We note that the asymmetry in intensity of the in-gap excitations at positive/negative bias is changing as the gate voltage is increased (i.e., when changing the exchange coupling). Furthermore, the gate voltage

can also be used to tune the phase transition from a doublet ground state on the left to an BCS-like singlet ground state on the right hand side. By applying a small perpendicular magnetic field, the proximity effect in the gold leads is suppressed. This leads to a broadening of the in-gap states (Fig. 3b) and to a quantum phase transition to the Kondo regime (Fig. 3d) at higher magnetic fields.

The thermocurrent measured simultaneously with the differential conductance is shown in Fig. 3e–h (for more details on thermopower measurements see supporting information). We observe that the bias-dependent I_{th} changes sign at bias voltages where the slope of the differential conductance, d^2I/dV^2, changes. The magnitude of I_{th} is proportional to d^2I/dV^2 and exhibits an enhancement near sharp features of the differential conductance (see Fig. 3e–h). At zero magnetic field, the maximum/minimum values of I_{th} are around 1 pA / -250 fA, respectively, and are at negative bias (bound state with negative energy with respect to the Fermi level). When a magnetic field is applied, the I_{th} maps change in shape and magnitude: while the bias dependent I_{th} changes sign 3 times in the YSR regime at $B = 0$ (Fig. 3e), it changes once in the Kondo regime (left-hand side of Fig. 3h). Furthermore, the maximum value of I_{th} at zero-bias in the stability diagrams shown in Fig. 3e–h decreases with increasing B and is reduced by a factor of ≈ 2.8 when going from 0 to 60 mT.

Using our cryogenic superconducting on-chip thermometers, we extract a temperature drop of $\Delta T = 105 \pm 15$ mK across the molecule and calculate the differential thermoelectric conductivity (differential
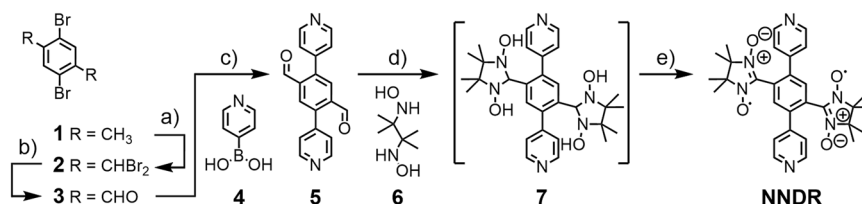
Fig. 4 | Synthesis of the nitronyl nitroxide di-radical (NNDR). Reagents and conditions: (**a**) NBS, BPO, DCE, reflux, 16 h, 98%; (**b**) AgNO$_3$, H$_2$O, EtOH, reflux, 1 h, 55%; (**c**) Pd(PPh$_3$)$_2$Cl$_2$, K$_2$CO$_3$, dioxane, MeOH, 80 °C, 15 h, 66%; (**d**) MeOH, reflux, 5 h, 75%; (**e**) NaIO$_4$, CHCl$_3$ (H$_2$O), room temperature, 1 h, 51%.

Seebeck coefficient) dS = dV_{th}/dT ≈ I_{th}/(dI/dV)/ΔT. We find a high dS = 470 μVK^{-1} at V_G = −2.71 V, V = −135 μV and B = 0. The quantum phase transition at finite magnetic fields reduces this maximum value by almost 50% to dS = 255 μVK^{-1} at V_G = −2.74 V, V = −200 μV at B = 60 mT. A similar enhancement by a factor of two originating from the presence of YSR states was found for the Seebeck coefficient, S_0 = dV_{th}/d$T|_{V=0}$, defined at zero bias voltage. We find S_0 = 154 μVK^{-1} at B = 0 and S_0 = 45 μVK^{-1} at 60 mT (i.e., in the Kondo regime). Furthermore, the corresponding power factor, $S_0^2 G$, at zero bias can be calculated (see Fig. 3i and Fig. S35). This value serves as a valuable indicator for assessing the efficiency of heat-to-energy conversion[25]. Our calculation reveals a five-fold enhancement by the YSR states to $S_0^2 G = 1.36 \times 10^{-4} \frac{k_{B2}}{\hbar}$, compared to $S_0^2 G = 0.27 \times 10^{-4} \frac{k_{B2}}{\hbar}$ in the Kondo regime.

Discussion

At small magnetic fields B > 60 mT, in the absence of superconductivity, gold is in its normal state and the system reveals the Kondo effect on the left-hand side of the CDP. From the Zeeman splitting (Fig. 2c), the temperature dependence of the width of the zero bias peak, and the shift of the CDP with magnetic field to more negative energies (see more details in the SI), we deduce that the molecule hosts an unpaired electron (S = 1/2). The extracted Kondo temperature $k_B T_K$ ≈ 70 μeV is greater than the typical values observed in GaAs quantum dots, yet aligns with the lower range associated with molecules[26]. Simultaneously, the tunnel coupling to the contacts exhibits notable asymmetry (from the Kondo analysis we extract a value of ≈1.2 × 10^4) that is frequently observed in electromigrated molecular junctions. Subsequently, the introduction of an additional electron to the system results in the disappearance of the zero-bias peak and changes the total spin of the molecule to zero (right-hand side of CDP).

When reducing B to zero, the gold undergoes a transition to proximity-induced superconductivity, resulting in a substantial reduction of the current within the bias window of the order of ± (Δ$_1$ + Δ$_2$)/e. However, in-gap excited states remain which originate from the interaction between proximity-induced quasi-particles on the contacts and the spin on the molecule. The high asymmetrical tunnel coupling to the contacts excludes the possibility that the peaks originate from Andreev multiple reflections because tunnel coupling asymmetries > 1 × 10^3 are typically sufficient to completely suppress them[27]. These arguments together with the large addition energy found in our sample (large-U regime, see Fig. S19), allows us to attribute the excitations to YSR states.

To further qualitatively describe the experimental data, we performed numerical simulations using the single impurity Anderson model[28] with one spin degenerate pair of quasi particles at energy Δ = 100 μeV, derived from a zero-bandwidth approximation (ZBW) fit[29]. The results of this calculation are shown in Fig. 1d as dotted green lines (see also Fig. S23). We find that the model describes the system's behavior with high fidelity and provides a comprehensive explanation for both the ground state and the observed excitations in the stability diagram: On the left side of the CDP, the system is in a doublet ground state, with its first excited state being the YSR

singlet. By adding an electron to the molecule, a phase transition from a doublet ground state to a BCS-like singlet is induced (right-hand side of the CDP). Here, the excited states take the form of a doublet. Since the system experiences weak coupling ($k_B T_K$ < Δ) it can be tuned from the YSR to a Kondo-like singlet via a doublet-singlet quantum phase transition by applying an external out-of-plane magnetic field, which predominately suppresses the superconducting gap and the exchange coupling (see Fig. 2a). According to numerical renormalization group theory (NRG) calculations[30] and experimental studies[31,32] this phase transition happens at $k_B T_K$/Δ ≈ 0.3 − 1, in agreement with the results presented here.

The quantum phase transition from YSR to Kondo physics has a strong impact on the thermoelectric response of the system. As observed earlier for single-molecule junctions in the Kondo regime[23], there is a correlation between the derivative (with respect to bias voltage) of the differential conductance and the thermocurrent, where sharp conductance features yield high thermoelectric response. Thus, since the sharpness of the conductance resonances depends on the magnetic field and temperature, we observe lower thermocurrent values as these parameters increase (Figs. 2d, 3). This ultimately results in a two fold increase of the Seebeck coefficient and a five-fold increase of the power factor when going through the quantum phase transition from Kondo to YSR.

In this work we performed thermoelectric transport measurements in an all organic diradical molecule coupled to proximity induced superconducting electrodes. The molecule plays the role of a spin-1/2 system with a high addition energy that, by interacting with the superconducting electrodes, leads to the presence of in-gap Yu-Shiba-Rusinov excitations. By applying a gate voltage, the charge on the molecule can be reproducibly changed from N − 1 to N, thereby inducing a phase transition from a doublet to singlet ground state. Applying an external magnetic field destroys the induced superconducting gap and drives a quantum phase transition from the YSR to the Kondo regime. This leads to a drastic decrease in the thermoelectric efficiency of the system. Thus, our work demonstrates that the efficiency of heat-to-energy conversion can be amplified by the presence of YSR states which act as sharp energy filters. While follow-up studies are required to investigate heat flow in such junctions, this work already provides information on how the power factor values can be boosted by in-gap states. By further optimizing parameters like the tunnel coupling strength, such molecular heat engines might posses thermoelectric efficiencies close to the theoretical limit.

Methods

Synthesis of NNDR

The 5-step synthesis of **NNDR** is displayed in Fig. 4. Synthetic protocols and analytical data are provided in the supporting information (Section 1, Supporting Figs. S1–S18). Starting with commercially available 2,5-dibromo-*para*-xylene (**1**), 2,5-dibromoterephthalaldehyde **3** was prepared in 54% yield over two steps by a fourfold bromination with N-bromosuccinimide (NBS) and benzoyl peroxide (BPO) in 1,2-dichloroethane (DCE) to provide **2**, which was transformed to **3** by silver nitrate promoted hydrolysis[33,34]. Twofold Suzuki cross coupling of dibromoterephthalaldehyde **3** with 4-pyridine boronic acid (**4**) gave

the dipyridyl rod **5** in moderate yield of 36%. The very limited solubility of **5** was not only challenging for its isolation, but also for its further processing. Following a literature procedure[35], the hydroxylamine **6** was prepared by reduction of the corresponding nitro derivative. For the condensation between **5** and **6**, the dipyridyl rod **5** was dissolved in boiling methanol before the hydroxylamine **6** was added. The diradical precursor **7** was obtained as insoluble white solid in a yield of 75%. The limited solubility of **7** compared to **NNDR** was particular challenging, as overoxidation of nitronyl nitroxide radicals to imino nitroxide derivatives is well known[36,37]. After extensive screening for suitable reaction conditions, a biphasic chloroform ($CHCl_3$) water system provided the desired **NDDR** in moderate yields. The precursor **7** was dispersed at 0 °C in degassed chloroform ($CHCl_3$) and after warm up to room temperature, aqueous sodium periodate ($NaIO_4$) was added dropwise. After stirring under protection gas atmosphere for one hour at room temperature, the crude reaction product was obtained by filtration through a silica plug. From the crude the target structure **NNDR** was obtained in 51% isolated yield as purple solid by reverse phase HPLC.

The diradical nature of **NNDR** was corroborated by its EPR spectrum, which shows 9 lines as expected for two delocalised unpaired electrons interacting with four equivalent ^{14}N nuclei in an isotropic manner. Temperature dependent EPR studies of **NNDR** and analytical data fully characterizing the target structure and all intermediates are provided in the supporting information.

Sample fabrication

The device is assembled on a Si wafer with a 285 nm layer of SiO_2 on top. All lithography steps are performed with electron beam lithography (Raith EBPG 5000+). Before each step, the sample is pretreated with acetone and isopropanol for one min. and spincoated with two layers of resist (8.5 MMA, 11% in Ethyl Lactate; 6000 rpm for 1 min.; baking at 180 °C for 5 min, and PMMA Solid 2% in Anisole, 950.0 molecular weight; 4000 rpm for 1 min.; baking at 180 °C for 3 min.). After lithography and development in MIBK : IPA = 1 : 3 for 90 s, the metals (Ti, Pd and Au) are deposited onto the structure by means of an e-beam evaporator (high vacuum around 10^{-8} mbar, evaporation rate of 0.5 Å/s) and molybdenum rhenium (MoRe, $T_C = 8.7\,K$, $\Delta \approx 1.3$ meV) superconducting contacts are sputtered with an AC450 Alliance system (RF generator power 100 W, process pressure 20 mbar, Ar flow 15 sccm).

A schematic design of the sample is depicted in Fig. 1a. It consists of a local gate (pink color) that is made by depositing a 1 nm thick adhesion layer of Ti and a 7 nm thick layer of Pd; two heaters (blue color) that are put together by evaporation 3 nm of Ti and 27 nm of Pd; 13 nm thick Au bridge (yellow color); and contacts (grey color) that are assembled by sputtering 100 nm MoRe. An insulating layer of 10 nm aluminum oxide, Al_2O_3, is deposited by atomic layer deposition in an Oxford Instruments FlexALD system (300 °C) right after the gate and heater deposition steps to form a dielectric for the gate and to prevent leakage from the heaters to the contacts.

Electromigration of the junction

Electromigration of golden junctions is performed by means of an active breaking scheme[38]. The idea behind the method is to increase the voltage across the junction via an ADwin GOLD box while simultaneously monitoring the resistance in an active feedback loop. The application of a high current density through the narrowest constriction induces electron momentum, which is sufficient to move the gold atoms, resulting in junction resistance modifications. Once the change of resistance reaches a specific value (cut-off parameter), the voltage is automatically reduced to zero and the ramping process is repeated. In such way the junction resistance is increased to 4 kΩ and then the junction is allowed to undergo self breaking[39] for approximately

10 min with further breaking during the subsequent molecular deposition and vacuum steps.

Molecular deposition

The molecule is dissolved in dichloromethane (DCM) with a 0.1 mM concentration and deposited on the chip right after electromigration via the drop-cast method. The molecule solution is freshly prepared and exposed to air only for a short amount of time while drop-casting it on the sample. To avoid self-breaking of the gold junctions to sizes that would exceed the molecular size (1–2 nm), the sample is thereafter immediately pumped to a low pressure and cooled down to low temperatures.

Simultaneous conductance and thermopower measurements

The measurements of conductance and thermocurrent are done simultaneously with a lock-in double-modulation technique[20] that is schematically illustrated in Fig. 1a. The differential conductance G, thermal current I_{th} and I_{DC} are measured by adding a small ac component ($V_{ac} = 5\,\mu V$) at a frequency $\omega_1 = 13$ Hz to bias voltage V_B, while an ac current through the heater at a frequency $\omega_2 = 3$ Hz is applied that creates an ac temperature bias proportional to Joule heating $\sim I_H^2$. The G is extracted from $\frac{I_{ac}}{V_{ac}}$, where the I_{ac} current is measured with a lock-in at ω_1, and the I_{th} is measured at $2\omega_2$. To determine the value of thermocurrent it is important to apply a correction factor of $-2\sqrt{2}$ to Y-component of the lock-in, recording the thermocurrent signal. This adjustment parameter arises from two factors: firstly, $\sqrt{2}$ from the fact that lock-in measures the root-mean-square voltage value and, secondly, -2 is attributed to the physical relationship between measured signal and ΔT that is proportional to $\sim I_H^2$. The ac measurements were conducted with $1\,\mu A$ current passing through the heater (440 Ω), which was the default setting employed through all stability measurements at 150 mK.

Thermometry

The temperature difference across the molecule is measured by means of SNS-thermometry[21]. First, both of the thermometers in the device are calibrated to the base temperature of the dilution refrigerator. Subsequently, the temperature on the different sides of the gold bridge is measured while a constant current is applied through the heater and the temperature gradient over the molecule is calculated. The calibration is done by collecting the distribution of 3000 switching currents and extracting the mean switching current value for different base temperatures (see Fig. S22). In order to decrease the amplitude of switching current, an AC triangular current signal at a frequency rate of 300 Hz is applied through the MoRe-Au-MoRe contact and the voltage response is recorded while the system is in equilibrium at base temperature in the presence of an 30 mT external magnetic field (see also calibration of thermometers and the more detailed discussion in the SI).

Data availability

The data that support the findings of this study are available under https://doi.org/10.4121/89ef5a5f-04c7-4e00-811e-541f3bddfe19.

References

1. Jaziri, N., Boughamoura, A., Müller, J., Mezghani, B., Tounsi, F. & Ismail, M. A comprehensive review of thermoelectric generators: Technologies and common applications. *Energy Rep.* **6**, 264–287 (2020).
2. Humphrey, T. E. & Linke, H. Quantum, cyclic, and particle-exchange heat engines. *Phys. E: Low.-dimensional Syst. Nanostruct.* **29**, 390–398 (2005).
3. Mahan, G. D. & Sofo, J. O. The best thermoelectric. *Proc. Natl Acad. Sci.* **93**, 7436–7439 (1996).

4. Josefsson, M., Svilans, A., Burke, A. M., Hoffmann, E. A., Fahlvik, S., Thelander, C., Leijnse, M. & Linke, H. A quantum-dot heat engine operating close to the thermodynamic efficiency limits. *Nat. Nanotechnol.* **13**, 920–924 (2018).

5. Mykkänen, E., Lehtinen, J. S., Grönberg, L., Shchepetov, A., Timofeev, A. V., Gunnarsson, D., Kemppinen, A., Manninen, A. J. & Prunnila, M. Thermionic junction devices utilizing phonon blocking. *Sci. Adv.* **6**, 9191 (2020).

6. Efetov, D. K., Wang, L., Handschin, C., Efetov, K. B., Shuang, J., Cava, R., Taniguchi, T., Watanabe, K., Hone, J., Dean, C. R. & Kim, P. Specular interband andreev reflections at van der waals interfaces between graphene and nbse2. *Nat. Phys.* **12**, 328–332 (2016).

7. Buitelaar, M. R., Belzig, W., Nussbaumer, T., Babic, B., Bruder, C. & Schönenberger, C. Multiple andreev reflections in a carbon nanotube quantum dot. *Phys. Rev. Lett.* **91**, 057005 (2003).

8. Hofstetter, L., Csonka, S., Nygård, J. & Schönenberger, C. Cooper pair splitter realized in a two-quantum-dot y-junction. *Nature* **461**, 960–963 (2009).

9. Das, A., Ronen, Y., Heiblum, M., Mahalu, D., Kretinin, A. V. & Shtrikman, H. High-efficiency cooper pair splitting demonstrated by two-particle conductance resonance and positive noise cross-correlation. *Nat. Commun.* **3**, 1165 (2012).

10. Kondo, J. Resistance Minimum in Dilute Magnetic Alloys. *Prog. Theor. Phys.* **32**, 37–49 (1964).

11. Yu, L. Bound state in superconductors with paramagnetic impurities. Wu Li Hsueh Pao (China) Supersedes Chung-Kuo Wu Li Hsueh For English translation see Chin. *J. Phys. (Peking) (Engl. Transl.)* **21**, 75–91 (1965).

12. Shiba, H. Classical Spins in Superconductors. *Prog. Theor. Phys.* **40**, 435–451 (1968).

13. Rusinov, A. I. Superconductivity near a paramagnetic impurity. *Sov. J. Exp. Theoretical Phys. Lett.* **9**, 85–87 (1969).

14. Yazdani, A., Jones, B. A., Lutz, C. P., Crommie, M. F. & Eigler, D. M. Probing the local effects of magnetic impurities on superconductivity. *Science* **275**, 1767–1770 (1997).

15. Ruby, M., Peng, Y., von Oppen, F., Heinrich, B. W. & Franke, K. J. Orbital picture of yu-shiba-rusinov multiplets. *Phys. Rev. Lett.* **117**, 186801 (2016).

16. Ji, S.-H., Zhang, T., Fu, Y.-S., Chen, X., Ma, X.-C., Li, J., Duan, W.-H., Jia, J.-F. & Xue, Q.-K. High-resolution scanning tunneling spectroscopy of magnetic impurity induced bound states in the superconducting gap of pb thin films. *Phys. Rev. Lett.* **100**, 226801 (2008).

17. Liebhaber, E., Rütten, L. M., Reecht, G., Steiner, J. F., Rohlf, S., Rossnagel, K., von Oppen, F. & Franke, K. J. Quantum spins and hybridization in artificially-constructed chains of magnetic adatoms on a superconductor. *Nat. Commun.* **13**, 2160 (2022).

18. Ruby, M., Heinrich, B. W., Peng, Y., von Oppen, F. & Franke, K. J. Wave-function hybridization in Yu-Shiba-Rusinov dimers. *Phys. Rev. Lett.* **120**, 156803 (2018).

19. Farinacci, L., Ahmadi, G., Reecht, G., Ruby, M., Bogdanoff, N., Peters, O., Heinrich, B. W., von Oppen, F. & Franke, K. J. Tuning the coupling of an individual magnetic impurity to a superconductor: Quantum phase transition and transport. *Phys. Rev. Lett.* **121**, 196803 (2018).

20. Gehring, P., Sowa, J. K., Hsu, C., de Bruijckere, J., van der Star, M., Le Roy, J. J., Bogani, L., Gauger, E. M. & van der Zant, H. S. J. Complete mapping of the thermoelectric properties of a single molecule. *Nat. Nanotechnol.* **16**, 426–430 (2021).

21. Volosheniuk, S., Bouwmeester, D., Hsu, C., van der Zant, H. S. J. & Gehring, P. Implementation of SNS thermometers into molecular devices for cryogenic thermoelectric experiments. *Appl. Phys. Lett.* **122**, 103501 (2023).

22. Roch, N., Florens, S., Bouchiat, V., Wernsdorfer, W. & Balestro, F. Quantum phase transition in a single-molecule quantum dot. *Nature* **453**, 633–637 (2008).

23. Hsu, C., Costi, T. A., Vogel, D., Wegeberg, C., Mayor, M., van der Zant, H. S. J. & Gehring, P. Magnetic-field universality of the Kondo effect revealed by thermocurrent spectroscopy. *Phys. Rev. Lett.* **128**, 147701 (2022).

24. Martin, I. & Mozyrsky, D. Nonequilibrium theory of tunneling into a localized state in a superconductor. *Phys. Rev. B* **90**, 100508 (2014).

25. Behnia, K. Fundamentals of thermoelectricity. Oxford University Press (2015).

26. Gehring, P., Thijssen, J. M. & van der Zant, H. S. J. Single-molecule quantum-transport phenomena in break junctions. *Nat. Rev. Phys.* **1**, 381–396 (2019).

27. Lee, E. J. H., Jiang, X., Aguado, R., Katsaros, G., Lieber, C. M. & De Franceschi, S. Zero-bias anomaly in a nanowire quantum dot coupled to superconductors. *Phys. Rev. Lett.* **109**, 186802 (2012).

28. Anderson, P. W. Localized magnetic states in metals. *Phys. Rev.* **124**, 41–53 (1961).

29. von Oppen, F. & Franke, K. J. Yu-shiba-rusinov states in real metals. *Phys. Rev. B* **103**, 205424 (2021).

30. Sakai, O., Shimizu, Y., Shiba, H. & Satori, K. Numerical renormalization group study of magnetic impurities in superconductors. II. dynamical excitation spectra and spatial variation of the order parameter. *J. Phys. Soc. Jpn.* **62**, 3181–3197 (1993).

31. Franke, K. J., Schulze, G. & Pascual, J. I. Competition of superconducting phenomena and kondo screening at the nanoscale. *Science* **332**, 940–944 (2011).

32. Island, J. O., Gaudenzi, R., de Bruijckere, J., Burzurí, E., Franco, C., Mas-Torrent, M., Rovira, C., Veciana, J., Klapwijk, T. M., Aguado, R. & van der Zant, H. S. J. Proximity-induced shiba states in a molecular junction. *Phys. Rev. Lett.* **118**, 117001 (2017).

33. Bodzioch, A. et al. Efficient synthesis of bis(dibromomethyl)arenes as important precursors of synthetically useful dialdehydes. *Synthesis* **48**, 3509–3514 (2016).

34. Bonifacio, M. C., Robertson, C. R., Jung, J.-Y. & King, B. T. Polycyclic aromatic hydrocarbons by ring-closing metathesis. *J. Org. Chem.* **70**, 8522–8526 (2005).

35. Hirel, C., Vostrikova, K. E., Pécaut, J., Ovcharenko, V. I. & Rey, P. Nitronyl and imino nitroxides: Improvement of ullman's procedure and report on a new efficient synthetic route. *Chem. - A Eur. J.* **7**, 2007–2014 (2001).

36. Wang, D., Ma, Y., Wolf, B., Kokorin, A. I. & Baumgarten, M. Temperature-dependent intramolecular spin coupling interactions of a flexible bridged nitronyl nitroxide biradical in solution. *J. Phys. Chem. A* **122**, 574–581 (2018).

37. Onal, E., Yerli, Y., Cosut, B., Pilet, G., Ahsen, V., Luneau, D. & Hirel, C. Nitronyl and imino nitroxide free radicals as precursors of magnetic phthalocyanine and porphyrin building blocks. *N. J. Chem.* **38**, 4440–4447 (2014).

38. van der Zant, H. S. J., Kervennic, Y.-V., Poot, M., O'Neill, K., de Groot, Z., Thijssen, J. M., Heersche, H. B., Stuhr-Hansen, N., Bjørnholm, T., Vanmaekelbergh, D., van Walree, C. A. & Jenneskens, L. W. Molecular three-terminal devices: fabrication and measurements. *Faraday Discuss.* **131**, 347–356 (2006).

39. O'Neill, K., Osorio, E. A. & van der Zant, H. S. J. Self-breaking in planar few-atom Au constrictions for nanometer-spaced electrodes. *Appl. Phys. Lett.* **90**, 133109 (2007).

Acknowledgements

Author contributions

H.S.J.v.d.Z., P.G. conceived and initiated the project. S.V. fabricated the devices, performed the electrical/thermoelectric measurement, and validated and analyzed the experimental data. D.B. implemented a theoretical model for sub-gap states and supported data analysis. D.V., C.W., and M.M. synthesized and characterized the molecule. C.H. supported the experiment. The experimental work was supervised by P.G. and H.S.J.v.d.Z. The manuscript was written through the contributions of all authors. All authors have approved the final version of the manuscript.

Competing interests

The authors declare no competing interests.

Additional information

Supplementary information The online version contains supplementary material available at https://doi.org/10.1038/s41467-025-58645-1.

Correspondence and requests for materials should be addressed to Herre S. J. van der Zant or Pascal Gehring.

Peer review information *Nature Communications* thanks Yingqiao Ma, and the other, anonymous, reviewer(s) for their contribution to the peer review of this work. A peer review file is available.

Reprints and permissions information is available at http://www.nature.com/reprints

Publisher's note Springer Nature remains neutral with regard to jurisdictional claims in published maps and institutional affiliations.